

# Large-Area Low-Cost Tunable Plasmonic Perfect Absorber in the Near Infrared by Colloidal Etching Lithography

Ramon Walter, Andreas Tittl, Audrey Berrier, Florian Sterl, Thomas Weiss, and Harald Giessen\*

Optical elements with absorbance close to unity are of crucial importance for diverse applications, ranging from thermal imaging to sensitive trace gas detection. A key factor for the performance of such devices is the need for absorbance with high acceptance angles, which are able to utilize all incident radiation from the forward-facing half-space. Here, a tunable, angle-, and polarization independent large-area perfect absorber is reported, which is fabricated by a combination of colloidal lithography and dry-etching. This design is easy and fast to produce, and low-cost compared with other common methods. Variation of the dry-etching time shifts the resonance from almost 825 to 1025 nm with reflection smaller than 3% and zero transmission. Due to the inherent disordered arrangement, this design is fully polarization independent and the absorbance remains higher than 98% for incident angles up to 50°.

absorbers or other complex plasmonic systems. Thus, for the production of sensors on an industrial scale, an easy and cheap fabrication method is necessary.

In this context, several large-area fabrication methods have already been demonstrated. One recent approach utilized silver nanocubes dispersed on a gold mirror covered with a polyelectrolyte spacer layer.<sup>[8]</sup> However, the precise synthesis of such nanocubes with a wide range of sizes can be challenging. Cosputtering of a metal–polymer composite on a spacer layer is also possible,<sup>[9]</sup> leading to broadband absorption and nearly perfect black absorbers.<sup>[10]</sup> Another method uses the controlled and low-rate deposition of a

very thin, noncontinuous metallic film to form metallic nanoislands on a dielectric spacer layer.<sup>[11,12]</sup> This allows for wafer-scale processing, but suffers from a very limited tuning range of the resonance wavelength.

A promising alternative approach is nanosphere lithography (NSL). NSL uses hexagonal close-packed nanospheres of polystyrene (PS)<sup>[13,14]</sup> or silica as masks for photolithography,<sup>[15]</sup> dry etching,<sup>[16–18]</sup> or evaporation.<sup>[19,20]</sup> Because of the hexagonal close-packed arrangement of nanospheres, this results in a similar array of nanostructures. Like all array-based perfect absorber geometries, such structures can exhibit grating effects, generally referred to as Rayleigh anomalies. Coupling of such grating modes to the perfect absorber resonance can reduce device performance, especially at higher incident angles.<sup>[21]</sup>

A similar approach is hole-mask lithography (HML),<sup>[22,23]</sup> where instead of forming a close-packed layer, the nanospheres are deposited on a sacrificial polymer film with well controlled but disperse particle separation. After evaporation of a thin metal film and removal of the nanospheres, cavities are etched into the polymer film. Normally, this is done with nondirectional oxygen plasma etching, leading to an undercut of the hole mask. Consequently, HML is a versatile method for large-area fabrication of many plasmonic structures such as disc-shaped structures, split-ring resonators,<sup>[24]</sup> or even chiral structures.<sup>[25]</sup>

However, HML is not well suited for the fabrication of large-area perfect absorbers, which require high surface coverage. In the high coverage case, the oxygen plasma treatment can completely etch away the polymer layer, resulting in the destruction of the mask. In addition, the sacrificial polymer layer is generally not very hydrophilic, making it difficult to achieve high nanosphere densities.

## 1. Introduction

A plasmonic nanostructure placed above a dielectric spacer and a metal mirror can act as an efficient absorber for incident light of a specific wavelength. By optimizing the structural parameters such as spacer layer thickness, shape, and size of the nanostructure, the absorption efficiency can be increased to nearly 100%, resulting in a perfect absorber. One prominent example of such a nanodevice utilizes a gold (Au) nanodisc above a magnesium fluoride (MgF<sub>2</sub>) spacer layer and a gold mirror to obtain perfect absorption in the near infrared.<sup>[1]</sup> Since then, the concept of plasmonic perfect absorption has been extended for many possible applications such as thermal imaging, photocatalysis, light trapping,<sup>[2]</sup> and sensing for gases,<sup>[3]</sup> proteins,<sup>[4]</sup> and polymers.<sup>[5]</sup> For many complex absorber designs, electron-beam lithography was the first choice for sample fabrication.<sup>[6,7]</sup> However, electron-beam lithography is expensive and requires very long processing times to produce arrays of structures on the order of 100 × 100 μm<sup>2</sup>. Consequently, it is nearly impossible to use this method for large-area fabrication of plasmonic perfect

R. Walter, A. Tittl, F. Sterl, Prof. T. Weiss, Prof. H. Giessen  
4th Physics Institute and Research Center SCoPE  
University of Stuttgart  
Pfaffenwaldring 57, 70550 Stuttgart, Germany  
E-mail: h.giessen@pi4.uni-stuttgart.de

Dr. A. Berrier  
1st Physics Institute and Research Center SCoPE  
University of Stuttgart  
Pfaffenwaldring 57, 70550 Stuttgart, Germany

DOI: 10.1002/adom.201400545



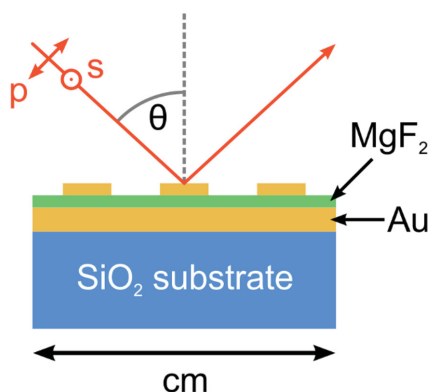


**Figure 1.** Sketch of the experimental setup. We perform angle-dependent reflectance measurements in s- and p-polarization.

Our approach combines advantages of colloidal lithography, such as disperse particle arrangement and large-area fabrication, with a dry etching process to produce a high performance large-area perfect absorber. Randomly dispersed, spatially separated PS nanospheres with a high surface coverage are deposited on a sacrificial metal layer and act as a mask for directional dry etching using an Argon (Ar) ion beam. Through a straightforward variation of the etching time, we can easily tune the resonance wavelength of our perfect absorber over a wide range. Measurements with different incident angles of the incoming light in s- and p-polarization (**Figure 1**) show that the absorption of our design remains extremely high, even at large incident angles.

## 2. Fabrication

The preparation process of the disperse Au nanodiscs required by our perfect absorber design is shown in **Figure 2**. In the first step, we use electron-beam-assisted evaporation to deposit the gold (Au) mirror, followed by the magnesium fluoride ( $\text{MgF}_2$ ) spacer layer. Starting from extensive numerical simulations (Figure S1a, Supporting Information) followed by iterative experimental optimization, we found that a spacer thickness of 50 nm yields the best results. On top of the spacer layer, we deposit another Au layer (with 20 nm thickness) and a sacrificial nickel (Ni) layer with 40 nm thickness. The Au nanodiscs required by our design are prepared from the upper Au layer via Ar dry etching. During the Ar etching process, most of the redeposited Au sticks to the sacrificial Ni layer, which can later be removed using wet etching.

As mask for the dry etching process, we use PS nanospheres with a diameter of 160 nm, as indicated by our simulations for resonances in the near-infrared regime (Figure S1b, Supporting Information). The PS nanospheres are dispersed on the Ni film by layer-by-layer deposition.<sup>[26,27]</sup> This step is analogous to the hole-mask fabrication described in refs. [22] and [23]. To obtain high surface coverage of the PS nanospheres, it is important to achieve smooth wetting of the surface with a polydiallyldimethylammonium chloride (PDDA) solution. PDDA possesses cathodic character and binds the PS nanospheres, which exhibit anionic character.

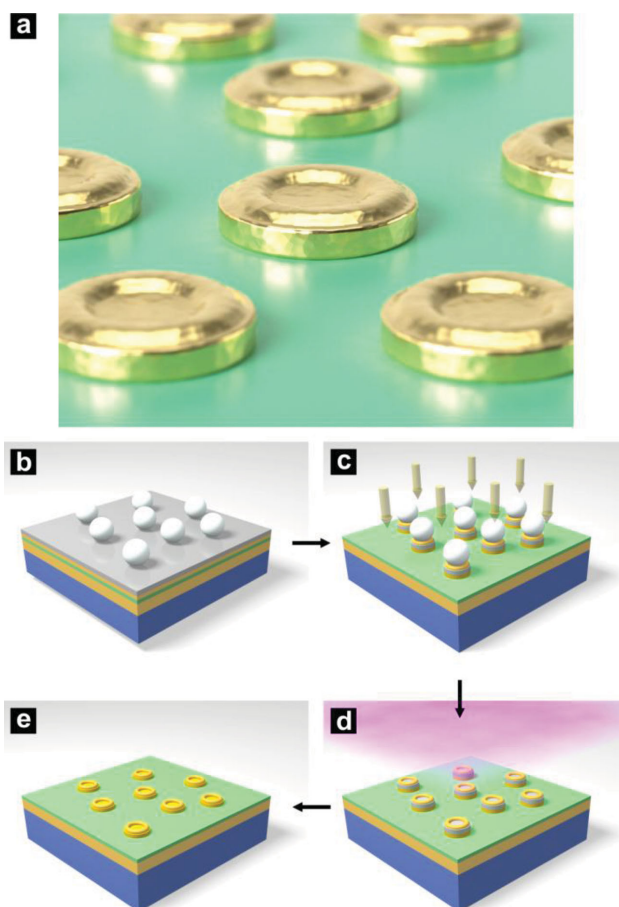


**Figure 2.** Sketch of the fabrication process of our large-area perfect absorber. a) Illustration of the final structure. b) Glass substrate after evaporation of the initial multilayer system, which incorporates a 100 nm gold (Au) mirror, 50 nm magnesium fluoride ( $\text{MgF}_2$ ) spacer layer, 20 nm Au, and a 40 nm nickel (Ni) sacrificial layer, and after the deposition of the polystyrene (PS) nanospheres. c) Dry etching process using directional argon (Ar) etching. d) Nanosphere removal using  $\text{O}_2$  plasma. e) The final structure after Ni removal via wet etching. It consists of Au nanodiscs above a  $\text{MgF}_2$  spacer layer and a gold mirror.

To improve the wetting, we expose the sacrificial Ni layer to  $\text{O}_2$  plasma for a few seconds. This procedure increases the hydrophilic properties of the layer and improves the wetting.

The mask is now ready for the dry etching process. During this process, the sample holder rotates continuously and is tilted by  $22^\circ$  with respect to the sample plane to reduce the amount of Au redeposition. This tilted etch also leads to smoother edges in the final nanostructured Au disks. Variations of the etching time have crucial influence on the resulting diameter of our nanodiscs and consequently on the resonance wavelength as depicted in **Figure 3a–e**. This allows us to tune the perfect absorber in a wavelength range of around 300 nm.

After a certain duration, longer etching times will not have any effect on structure size anymore without increasing the tilt angle. The diameter and hence the resonance wavelength show a lower limit because the PS nanospheres will shadow the Au film below and protect an Au disk of minimum size from the etching process.

After the dry etching, the PS nanospheres are removed by immersion in acetone for several hours, and afterwards the

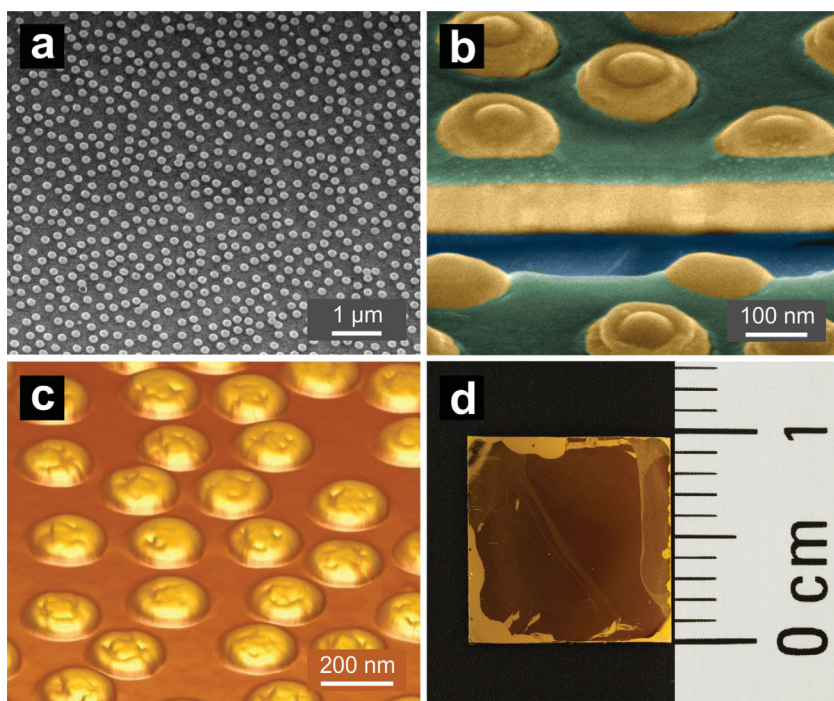


**Figure 3.** Micro- and macrostructural characterization of the large-area perfect absorber structures. a) SEM image of the fabricated structure. A disperse, disordered, and nearly defect-free arrangement of nanodiscs is clearly visible on the sample. b) Focused ion beam cut through the sample. The initial material layer structure is maintained, and the disks are defined with only slight etching into the  $\text{MgF}_2$  spacer layer. The yellow color represents gold,  $\text{MgF}_2$  is green, and the substrate is shown in blue. c) Atomic force microscopy (AFM) image of the sample, displaying the homogeneous height distribution of individual nanodiscs. d) Optical image of a full  $10 \times 10 \text{ mm}^2$  sample. The structured area (dark regions) covers nearly the complete surface of the sample.

sample is treated in  $\text{O}_2$  plasma to make sure that all of the PS is gone. The remaining Ni is removed with diluted sulfuric acid. The resulting perfect absorber structures exhibit a surface coverage of about 26%, as evident from scanning electron microscopy (SEM) images (Figure 3a). Further statistical analysis shows an average interparticle distance of 285 nm with a standard deviation of 80 nm. This results in mostly uncoupled Au nanodiscs (Figure S2, Supporting Information).

To examine the vertical composition of our perfect absorber, we perform a focused ion beam (FIB) cut through the sample, and then image the resulting edge using SEM (Figure 3b). It is clearly visible that the initial material layer structure (Au,  $\text{MgF}_2$ ) is well maintained, and the Au nanodiscs are defined with only slight etching damage of the  $\text{MgF}_2$  spacer layer. In addition, we use atomic force microscopy (AFM) to study the height profile of the fabricated nanodiscs and observe a very homogeneous height distribution of the individual disks (Figure 3c). One key advantage of our method is the ability to structure large areas up to several  $\text{cm}^2$  easily and reliably (Figure 3d).

### 3. Results and Discussion

Figure 4a shows the optical near-infrared spectra of four-fabricated perfect absorber structures with different dry etching times. To minimize the influence of variations in the etching

rates, all samples were etched simultaneously and removed step-by-step after a specific time. The red lines show the results after an etch time of 240 s, measured at two randomly chosen positions. The resonance wavelength is located at around 1010 nm and the reflectance is very low with a value of around 0.8%.

With longer etching times, the Au nanodiscs become smaller and the resonance position shifts to the blue. The blue lines represent a sample etched for a total of 270 s. The resonance is now located at around 937 nm, while the reflectance is still extremely low at around 1.7%. Increasing the etching time further, the green and black lines represent a sample with 300 and 330 s. For 300 s, the resonance wavelength shifts to around 867 nm with a reflectance of around 2.3%. The last design (black lines) exhibits its resonance at around 836 nm with a reflectance of around 1.5%.

The corresponding SEM images (Figure 4b–e) indicate that with decreasing etching time the diameter of the nanodiscs is becoming bigger. A larger diameter of the nanodiscs also leads to a longer resonance wavelength of the plasmon oscillation inside the disk.

Optical spectra with varied incidence angles are shown in Figure 5a for s-polarization and in Figure 5b for p-polarization. The sample was etched for 250 s. In s-polarization, the reflectance remains very low even when the incident angle  $\theta$  increases. The

highest reflectance was measured for  $\theta = 20^\circ$  with 1.7%, the lowest for  $\theta = 40^\circ$  with 0.3%. The resonance wavelength undergoes a slight shift to the red, from 980 ( $\theta = 20^\circ$ ) to 1000 nm ( $\theta = 50^\circ$ ).

In p-polarization, the resonance shifts to the blue with increasing incident angle  $\theta$ . For  $\theta = 20^\circ$  the resonance is located at 980 nm, while the reflectance is at 1.8%. For an incident angle of  $\theta = 50^\circ$  the resonance shifts blue to 930 nm while the reflectance remains very low at 0.3%.

As discussed by Dayal and Ramakrishna,<sup>[28]</sup> we expect a perfect absorber with disk-shaped nanostructures to be independent of the polarization of the incoming light and of variations of the incident angle from around  $-25^\circ$  to  $25^\circ$ . With incident angle  $\theta = 0^\circ$  the vector of the electric field  $\mathbf{E}$  of the incoming light is always parallel to the surface of the disk in s- and in p-polarization. Thus, the resonant plasmonic oscillation in the disk structure will always be perpendicular to the pointing vector  $\mathbf{S}$  and parallel to the gold mirror. This behavior is also clearly visible in simulations of the local electric near field. Figure 6a,b shows the simulated electric field distribution between the nanodisc and the mirror at normal incidence for s- and p-polarization, respectively. The field distributions are identical in both cases, apart from the direction of the plasmon oscillations.

Changing  $\theta$  will lead to different effects with regard to the polarization of the incident light. In s-polarization and

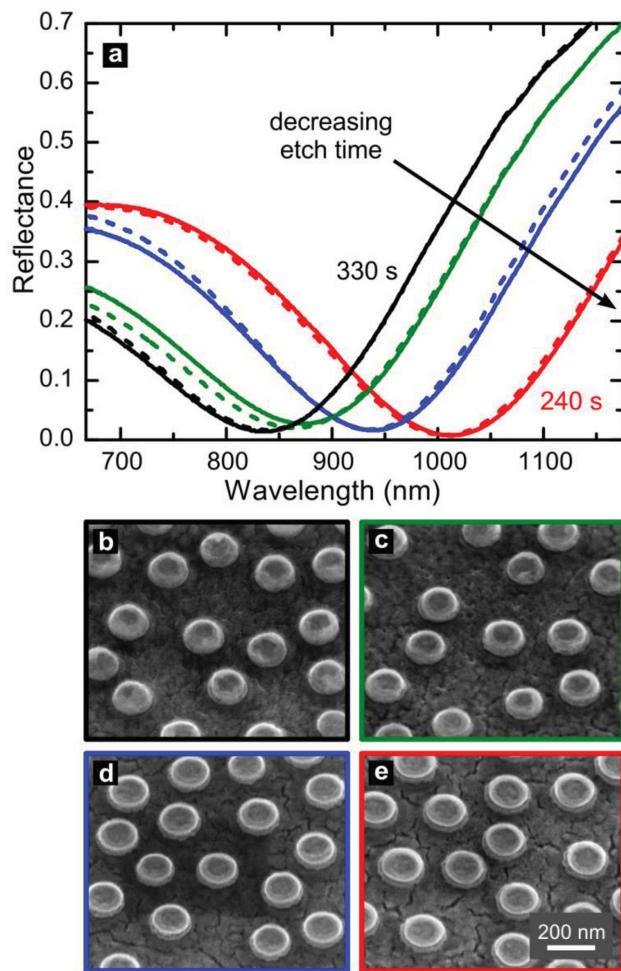


**Figure 4.** Spectral tunability of the perfect absorber resonance wavelength. a) The wavelength of perfect absorption can be tuned from  $\approx 825$  to 1025 nm through a straightforward variation of the Ar etch time. b–e) SEM images of the perfect absorber structures from (a). The increase of the disk size when going from higher (330 s) (b) to lower (240 s) (e) etch times in steps by 30 s is clearly visible.

under-angled incidence,  $\mathbf{E}$  will only excite the in-plane component of the plasmon resonance, while p-polarized light will also excite the perpendicular component of the plasmon resonance.

The fact that the absorbance is reduced with increasing  $\Theta$  in s-polarization while in p-polarization the absorbance is still high is well known.<sup>[29,30]</sup> At resonance, the currents in the nanodisc and in the gold mirror are antiparallel. This results in a magnetic moment, which interacts with the magnetic field of the incident light. Importantly, in p-polarization the orientation of the magnetic field  $\mathbf{B}$  is more or less the same while in s-polarization the orientation changes with the incident angle. Thus, the interaction between the magnetic moment and the magnetic field of the incident light is reduced, the magnetic field cannot couple to the circulation current efficiently with increasing  $\Theta$ , and more light is reflected back.

In p-polarization, Figure 5b shows an obvious experimental blueshift of the resonance with increasing  $\Theta$  in accordance with Withayachumnankul et al.<sup>[30]</sup> Here, the vertical component of  $\mathbf{E}$  increases, while the horizontal component decreases.

To understand the influence of this effect on the resonance wavelength, we consider each nanodisc as an arrangement of discrete dipoles, a well-established technique known as discrete dipole approximation. When excited under an angle, the discrete dipoles in the nanodisc no longer oscillate in phase over the whole disk because the wave front of the incoming light does not strike the whole nanodisc simultaneously. This phase delay leads to a reduced coupling of the individual dipole moments in the disk, which results in an increase of the system's energy and consequently a blueshift of the resonance wavelength.<sup>[31]</sup> For normal incidence, the wave front of the incoming light is parallel to the disk surface. Accordingly, all discrete dipoles are excited in phase and the system oscillates in a lower energy state.

This is also supported by our numerical simulations in Figure 6c,d, which show a clear imbalance of the charge density in the structure for larger incident angles.

In s-polarization, the orientation of  $\mathbf{E}$  is independent of the incident angle and constant. Thus,  $\mathbf{E}$  excites the discrete dipoles in phase, as in the case of  $\Theta = 0^\circ$ . This implies a balanced charge density in the nanodisc, resulting in fully wavelength stable absorption.

#### 4. Conclusion

We have demonstrated a straightforward, low cost, and high-throughput method to fabricate large-area plasmonic perfect absorber devices in the near infrared by using PS nanospheres as a dry etching mask. Our method allows spectral tuning of the resonance wavelength via a variation of the etching time. Our method is versatile, and can easily be extended to other wavelength ranges, simply by using different PS nanospheres with varying diameters. With Fourier transformation-infrared spectrometer (FTIR)- and angle-resolved reflectance measurements, we have shown that the absorption of our devices remains extremely high in all polarizations, and even at large incident angle  $\Theta$ . Our design is independent of the polarization at normal incidence. With increasing incident angle and p-polarized light, the resonance wavelength shifts to blue because of delayed excitation of the plasmon oscillations, while the residual reflectance remains very low.

Since we are not using any material specific processing steps, our method can easily be used with other materials instead of the well-known Au-MgF<sub>2</sub> system. Thus, our fabrication method can be used for a variety of applications and material systems, ranging from gas and chemical sensing to enhanced photovoltaics.

#### 5. Experimental Section

Borosilicate substrates (Menzel-Gläser,  $10 \times 10 \text{ mm}^2$ ) are cleaned with acetone for 5 min in an ultrasonic bath, then rinsed with isopropyl alcohol and demineralized water, and blow dried with nitrogen (N<sub>2</sub>).

All necessary materials are evaporated using an electron-beam-assisted evaporation machine (Pfeiffer PLS500). For the mirror, we used 5 nm of titanium (Ti) as adhesion layer, followed by 120 nm of Au. For the spacer layer, 50 nm of MgF<sub>2</sub> are evaporated onto the mirror, followed by another 20 nm of Au and 40 nm of Ni as sacrificial layer. After this,

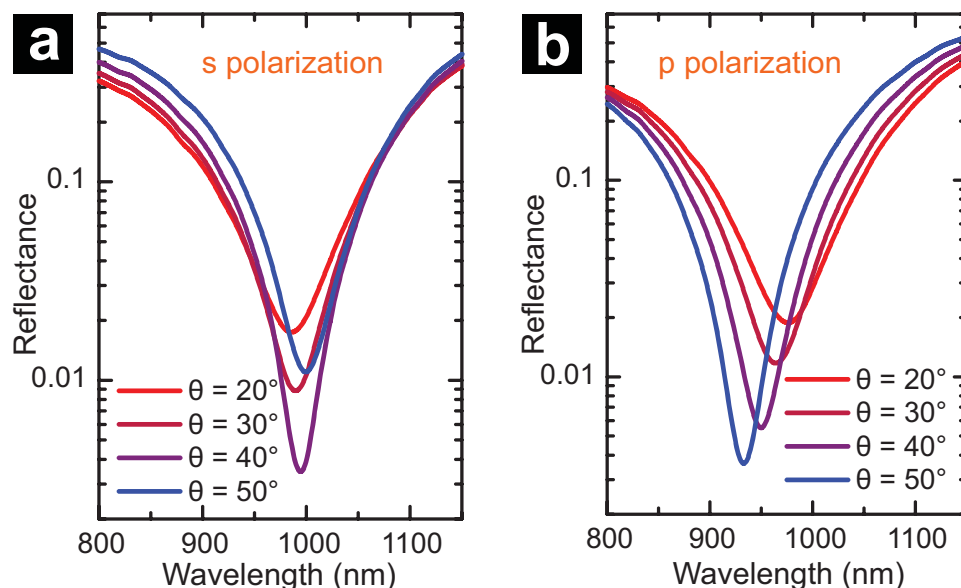


**Figure 5.** Angle-resolved reflectance measurements in s- and p-polarization. For both polarizations, the reflectance remains below 2% for angles up to 50°. a) In s-polarization, the spectral location of lowest reflectance stays mostly constant, with only a slight redshift for higher incident angles. b) In p-polarization, the resonance wavelength undergoes a blueshift of up to 50 nm for higher angles. This is due to an increasing asymmetry in the charge distribution of the plasmonic disk.

we store the sample for one day in a nitrogen chamber to give the MgF<sub>2</sub> enough time to recrystallize.

To improve the hydrophilic character of the Ni layer, the surface is treated in an O<sub>2</sub> plasma for 18 s (Diener Pico, 0.5 mbar, power level 100 W, HF power at 2.45 GHz). After this, a solution of PDPA

(Sigma–Aldrich, 0.2 wt% in water) is immediately drop coated on the Ni surface. Next, the sample is rinsed with demineralized water and dried with N<sub>2</sub>. Directly after this step, PS nanospheres (from Banglabs, 160 nm diameter, nonfunctionalized, 0.2 wt% in water, ultrasonicated for about 40 min) are drop coated on the surface, rinsed after 1 min with

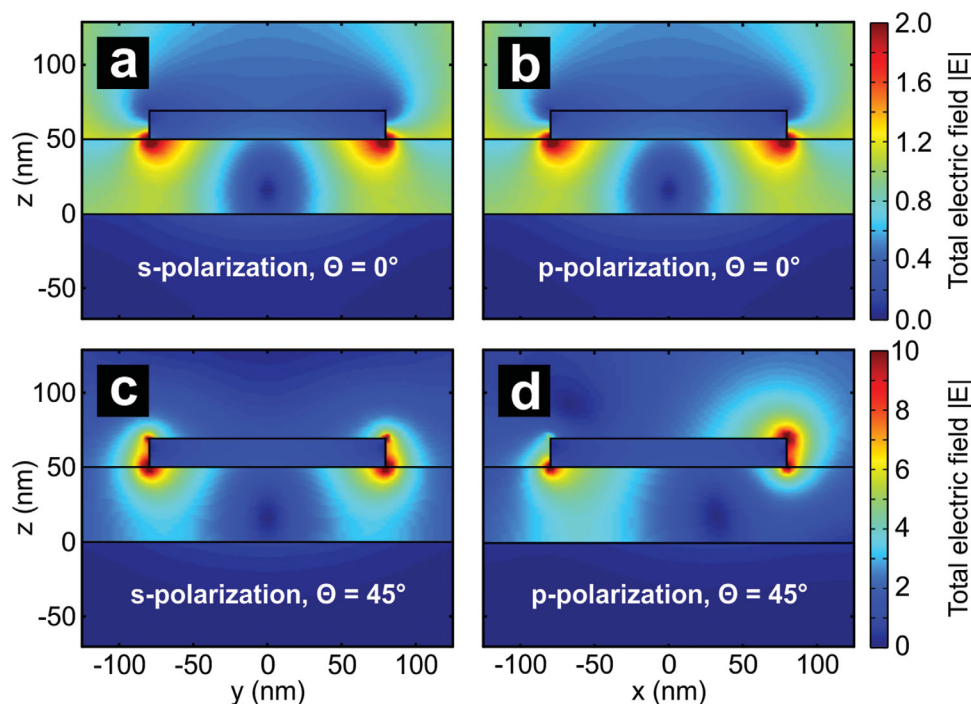


**Figure 6.** Calculated electric near-field intensity for s- and p-polarized incident light at incident angle  $\Theta = 0^\circ$  and  $\Theta = 45^\circ$ . For incident angle  $\Theta = 0^\circ$ , the field distribution for a) s- and b) p-polarization is identical except for a change in the direction of the plasmon oscillation. With increasing  $\Theta$ , the difference between both polarizations increases. c) Calculated field for s-polarization with  $\Theta = 45^\circ$ . The field remains well balanced and qualitatively similar to the normal incidence case. d) For p-polarization, the orientation of the incident E-field with regard to the sample surface changes, leading to an imbalance of the charge distribution and thus a spectral blueshift for increasing angles.

demineralized water and immersed in hot water (98 °C) for about 3 min. After this, the samples are dried with N<sub>2</sub>. The samples are now covered with PS nanospheres in a random arrangement. The surface coverage is calculated with a MATLAB script from an SEM image.

To produce the nanodiscs, the samples are glued on the sample holder of R.I.B.-Etch 160 from Technics Plasma and etched with Ar (20%) with a tilted and rotating sample holder (tilt angle  $\alpha = 20^\circ$ ) for a specified time (240–330 s).

The PS nanospheres are removed by putting the samples in acetone for about 12 h, followed by treatment in O<sub>2</sub> plasma for 30 min (Diener Pico, 1.6 mbar, power level 200 W, HF power at 2.45 GHz).

Concentrated sulfuric acid (Merck, 98%) is diluted 1:9 with demineralized water. The sample is put into the acid for 2 min, rinsed afterwards with demineralized water, and dried with N<sub>2</sub>.

SEM measurements are carried out with a Hitachi S4800 and the F.I.B cut with a FEI Helios NanoLab 600. AFM measurements are performed in tapping mode in air with a Veeco Dimension Icon in combination with NanoAndMore TAP300-AR-G-50 tips. For analysis of the AFM measurements, we used the Software NanoScope Analysis from Bruker in Version 1.40.

For optical measurements, we use a FTIR from Bruker (Vertex-80) attached to an IR microscope (Bruker Hyperion II). As detector, we used a silicon (Si) diode and a CaF<sub>2</sub>-UV-NIR beamsplitter. As reference, we used a dielectric broadband mirror from Thorlabs (BB1-E03, 750–1100 nm). The measurements were taken in reflection with 200 scans and a resolution of 16 cm<sup>-1</sup>. For polarization dependent measurement we used a near-infrared polarizer.

The angle-resolved intensity measurements are performed in reflection in the wavelength range from 600 to 1300 nm, using a Woollam ellipsometer setup. The light source is a xenon arc lamp associated with a monochromator. The light beam is collimated and has a diameter of about 2 mm. The incident angle was varied between 0° and 50° in steps of 10°. As reference, a Herasil sample was used.

For simulation of the electric near-field distributions, we used CST Studio Suite 2014 in Release Version 2014.02. The gold disk is defined with a diameter of 160 nm and a thickness of 20 nm. We set the thickness of the MgF<sub>2</sub> spacer to 50 nm and the thickness of the gold mirror to 120 nm. To avoid interferences from the boundary conditions we set the length and the width of spacer and mirror to 1000 nm. Field calculations were carried out in the frequency domain at a resonance frequency of 345 THz.

Periodic array-based simulations are done with a scattering-matrix-based Fourier modal method.<sup>[32,33]</sup> As parameters we set the spacer thickness to 30 nm, the periodicity to 350 nm and we varied the disk diameter from 120 to 200 nm and the wavelength from 600 to 1200 nm.

## Acknowledgements

The authors gratefully acknowledge financial support by the Deutsche Forschungsgemeinschaft (SPP1391, FOR730, GI 269/11–1), the Bundesministerium für Bildung und Forschung (13N9048 and 13N10146), the ERC Advanced Grant COMPLEXPLAS, the Baden-Württemberg Stiftung (PROTEINSENS, Spitzenforschung II), the Carl-Zeiss Foundation, the Alexander von Humboldt-Foundation, and the Ministerium für Wissenschaft, Forschung und Kunst Baden-Württemberg (Az: 7533–7–11.6–8). They acknowledge technical assistance by M. Ubl, and useful discussions with N. Strohfeldt, S. Bagheri, and F. Neubrech. They also thank L. Fu for the FIB cut, and D. Flöss for the photography.

Received: November 12, 2014  
Published online: January 2, 2015

- [1] N. Liu, M. Mesch, T. Weiss, M. Hentschel, H. Giessen, *Nano Lett.* **2010**, *10*, 2342.
- [2] F. Yu, H. Wang, S. Zou, *J. Phys. Chem. C* **2010**, *114*, 2066.
- [3] A. Tittl, P. Mai, R. Taubert, D. Dregely, N. Liu, H. Giessen, *Nano Lett.* **2011**, *11*, 4366.
- [4] Y. Li, L. Su, C. Shou, C. Yu, J. Deng, Y. Fang, *Sci. Rep.* **2013**, *3*, 2865.
- [5] K. Chen, R. Adato, H. Altug, *ACS Nano* **2012**, *6*, 7998.
- [6] N. I. Landy, S. Sajuyigbe, J. J. Mock, D. R. Smith, W. J. Padilla, *Phys. Rev. Lett.* **2008**, *100*, 207402.
- [7] H. Tao, N. I. Landy, C. M. Bingham, X. Zhang, R. D. Averitt, W. J. Padilla, *Opt. Express* **2008**, *16*, 7181.
- [8] A. Moreau, C. Cirac, J. J. Mock, R. T. Hill, Q. Wang, B. J. Wiley, A. Chilkoti, D. R. Smith, *Nature* **2012**, *492*, 86.
- [9] M. K. Hedayati, F. Faupel, M. Elbahri, *Appl. Phys. A* **2012**, *109*, 769.
- [10] M. K. Hedayati, M. Javaherirahim, B. Mozooni, R. Abdelaziz, A. Tavassolizadeh, V. S. K. Chakravadhanula, V. Zaporojtchenko, T. Strunkus, F. Faupel, M. Elbahri, *Adv. Mater.* **2011**, *23*, 5410.
- [11] D. Wang, W. Zhu, M. D. Best, J. P. Camden, K. B. Crozier, *Sci. Rep.* **2013**, *3*, 2867.
- [12] Y. Zhang, T. Wei, W. Dong, K. Zhang, Y. Sun, X. Chen, N. Dai, *Sci. Rep.* **2014**, *4*, 4850.
- [13] A. Kosiorek, W. Kandulski, H. Glaczynska, M. Giersig, *Small* **2005**, *1*, 439.
- [14] P. Pieranski, *Phys. Rev. Lett.* **1980**, *45*, 569.
- [15] W. Wu, D. Dey, O. G. Memis, A. Katsnelson, H. Mohseni, *Nanoscale Res. Lett.* **2008**, *3*, 351.
- [16] D.-G. Choi, H. K. Yu, S. G. Jang, S.-M. Yang, *J. Am. Chem. Soc.* **2004**, *126*, 7019.
- [17] S.-H. Hong, J.-H. Shin, B.-J. Bae, H. Lee, *Jpn. J. Appl. Phys.* **2011**, *50*, 036501.
- [18] S. Law, L. Yu, A. Rosenberg, D. Wasserman, *Nano Lett.* **2013**, *13*, 4569.
- [19] M. C. Gwinner, E. Koroknay, L. Fu, P. Patoka, W. Kandulski, M. Giersig, H. Giessen, *Small* **2009**, *5*, 400.
- [20] G. Zhang, D. Wang, *Chem Asian J.* **2009**, *4*, 236.
- [21] A. Tittl, M. G. Harats, R. Walter, X. Yin, M. Schäferling, N. Liu, R. Rapaport, H. Giessen, *ACS Nano* **2014**, *8*, 10885.
- [22] S. Cataldo, J. Zhao, F. Neubrech, B. Frank, C. Zhang, P. V. Braun, H. Giessen, *ACS Nano* **2011**, *6*, 979.
- [23] H. Fredriksson, Y. Alaverdyan, A. Dmitriev, C. Langhammer, D. S. Sutherland, M. Zäch, B. Kasemo, *Adv. Mater.* **2007**, *19*, 4297.
- [24] J. Zhao, C. Zhang, P. V. Braun, H. Giessen, *Adv. Mater.* **2012**, *24*, OP247.
- [25] B. Frank, X. Yin, M. Schäferling, J. Zhao, S. M. Hein, P. V. Braun, H. Giessen, *ACS Nano* **2013**, *7*, 6321.
- [26] G. Decher, J. B. Schlenoff, *Multilayer Thin Films: Sequential Assembly of Nanocomposite Materials*, Wiley-VCH, Weinheim, Germany **2012**.
- [27] G. Decher, *Science* **1997**, *277*, 1232.
- [28] G. Dayal, S. A. Ramakrishna, *Opt. Express* **2012**, *20*, 17503.
- [29] J. Hao, L. Zhou, M. Qiu, *Phys. Rev. B* **2011**, *83*, 165107.
- [30] W. Withayachumnankul, C. M. Shah, C. Fumeaux, B. S. -Y. Ung, W. Padilla, M. Bhaskaran, D. Abbott, S. Sriram, *ACS Photonics* **2014**, *1*, 625.
- [31] N. Liu, H. Giessen, *Angew. Chem.* **2010**, *122*, 10034.
- [32] T. Weiss, G. Granet, N. A. Gippius, S. G. Tikhodeev, H. Giessen, *Opt. Express* **2009**, *17*, 8051.
- [33] T. Weiss, N. A. Gippius, S. G. Tikhodeev, G. Granet, H. Giessen, *J. Opt. A: Pure Appl. Opt.* **2009**, *11*, 114019.